frontiers | Frontiers in Earth Science

TYPE Original Research
PUBLISHED 09 May 2023
DOI 10.3389/feart.2023.1164162

OPEN ACCESS

EDITED BY
Songjian Ao,
Institute of Geology and Geophysics (CAS), China

REVIEWED BY
Rongguo Zheng,
Chinese Academy of Geological Sciences (CAGS), China
Fanchao Meng,
China University of Petroleum, China

*CORRESPONDENCE
Keyong Wang,
wkyong@163.com

RECEIVED 12 February 2023
ACCEPTED 13 April 2023
PUBLISHED 09 May 2023

CITATION
Cai H, Gong X, Liu G, Guo R and Wang K (2023), Triassic magmatism and tectonic setting of Eastern Tianshan, NW China: constraints from the geochemistry and zircon U–Pb–Hf isotopes of granitoids in the Yamansu area.
Front. Earth Sci. 11:1164162.
doi: 10.3389/feart.2023.1164162

Triassic magmatism and tectonic setting of Eastern Tianshan, NW China: constraints from the geochemistry and zircon U–Pb–Hf isotopes of granitoids in the Yamansu area

Hongming Cai[1,2,3], Xiangkuan Gong[1], Guiping Liu[1], Ruiqing Guo[1] and Keyong Wang[1]*

[1]School of Geology and Mining Engineering, Xinjiang University, Urumqi, China, [2]Geography Postdoctoral Research Station, Xinjiang University, Urumqi, China, [3]Xinjiang Key Laboratory for Geodynamic Processes and Metallogenic Prognosis of the Central Asian Orogenic Belt, Xinjiang University, Urumqi, China

Introduction: To provide constraints on the Triassic tectonic setting of Eastern Tianshan, an integrated study was conducted on the geochronological and geochemical data for granodiorites, monzogranites, and two-mica granites from the Yamansu area on the northern margin of the Central Tianshan, NW China.

Geochronlogy Method and Results: Zircon U–Pb dating indicated the crystallization ages of ca. 250–241 Ma.

Geochemistry Results: The granodiorites (ca. 250 Ma) were medium-K calc-alkaline I-type granitoids, with crust-derived geochemical elements ratios (e.g., Ti/Zr, Ti/Y, and Nb/Ta), low Sr/Y ratios, and moderate negative Eu anomalies (Eu/Eu* = 0.56–0.57), suggesting their derivation from the partial melting of crustal materials with plagioclase as a major residual phase at <12 kbar. The monzogranites (ca. 247 Ma) showed adakitic characteristics, with high SiO_2 and low MgO, Cr, and Ni contents and low Nb/Ta ratios, indicating an origin from the melting of thickened mafic lower crusts at relatively high pressure (12–15 kbar). The ca. 244 Ma and ca. 241 Ma two-mica granites were high-K calc-alkaline and showed geochemical features of highly fractionated I-type granites. They were generated by melting medium-to-high-K mafic to intermediate crustal rocks at pressures <5 kbar, accompanied mainly by feldspar fractional crystallization. All granitoids had zircon $\varepsilon_{Hf}(t)$ values of +7.8 to +2.1, with corresponding T_{DM2} of 1132–773 Ma, suggesting juvenile crustal rocks as possible sources.

Discussion: Geochronological investigations of the studied granitoids, together with published data, suggest that the Triassic was an important period for granitic magmatism in Eastern Tianshan. Considering all the available geological data, we suggest that the Triassic granitoids were formed in an intracontinental environment possibly controlled mainly by far-field effects of the Paleo-Tethys system, with contemporaneous compression and extension at deep and shallower lithosphere depths, respectively, during the Triassic.

KEYWORDS

Triassic granitoids, geochemistry, petrogenesis, tectonic setting, Eastern Tianshan

1 Introduction

The Eastern Tianshan in Xinjiang, NW China, situated on the southern margin of the Central Asian Orogenic Belt (CAOB) (Figure 1A; Su et al., 2011), underwent a complex tectonic evolution involving subduction, accretion, collision, post-collisional/orogenic extension, and ensuing intracontinental process during the evolution of the Paleo-Asian Ocean system (Zhou et al., 2010; Xiao et al., 2013; Han and Zhao, 2018). Corresponding to the different tectonic stages, granitic intrusions with different geological and geochemical features were produced (Zhou et al., 2010; Wang et al., 2014; Zhang et al., 2015; Zhao et al., 2019; Long et al., 2020). These provide important constraints on the geodynamic environment during their emplacement, informing our understanding of the tectonic evolutionary history of Eastern Tianshan and its adjacent areas (Zhou et al., 2010; Dong et al., 2011; Ma et al., 2014). Most studies of this region have focused on the rocks formed in the Late Paleozoic (Dong et al., 2011; Ma et al., 2014; Zhang et al., 2015; Li et al., 2016), while those that occurred in the Triassic have received little attention. This restricts understanding of the Mesozoic magmatic-tectonic processes of Eastern Tianshan.

Recently, several Triassic granitic intrusions were identified in Eastern Tianshan (Zhang et al., 2017; Zhao et al., 2019; Muhtar et al., 2020; Lei et al., 2021; Zhi et al., 2021; Chen et al., 2022). However, the detailed geodynamic setting for the Triassic magmatism remains controversial, with various possible models including 1) a transition from subduction to post-subduction continental collision (Xiao et al., 2008; Mao et al., 2022), 2) a continental collision regime (Wu et al., 2013), 3) a tectonic transition from collisional crust shortening and thickening to post-collisional extension and thinning (Deng et al., 2017), 4) a post-collisional/orogenic extensional setting subsequent to termination of the Paleo-Asia Ocean (Li et al., 2013; Han et al., 2014; Wang et al., 2016; Wu et al., 2017), and 5) intra-continental extension or compression (Zhang et al., 2008; Wu et al., 2010; Wang et al., 2015a; Zhang et al., 2015; Zhang et al., 2017; Zhao et al., 2017; Chen et al., 2018; Zhao et al., 2019; Feng and Zheng, 2021; Lei et al., 2021; Chen et al., 2022). Therefore, further research on Triassic granitoids is urgently needed to constrain the geological setting of the region.

Recent field geological observations have suggested the existence of several Triassic granitoid intrusions in the southern part of Eastern Tianshan (south of the Yamansu area in Xinjiang, NW China) (Figure 1B; BGMRXUAR (Bureau of Geology and Mineral Resources of Xinjiang Uygur Autonomous Region), 2013). We present the first systematic study of the geology, whole rock geochemistry, zircon U–Pb, and Lu–Hf isotopic compositions for these granitoids. Furthermore, we use these data to constrain their ages, petrogenesis, and tectonic settings. In combination with previous findings, this study also provides new insights into the Triassic magmatism and the poorly constrained Triassic geological setting of Eastern Tianshan.

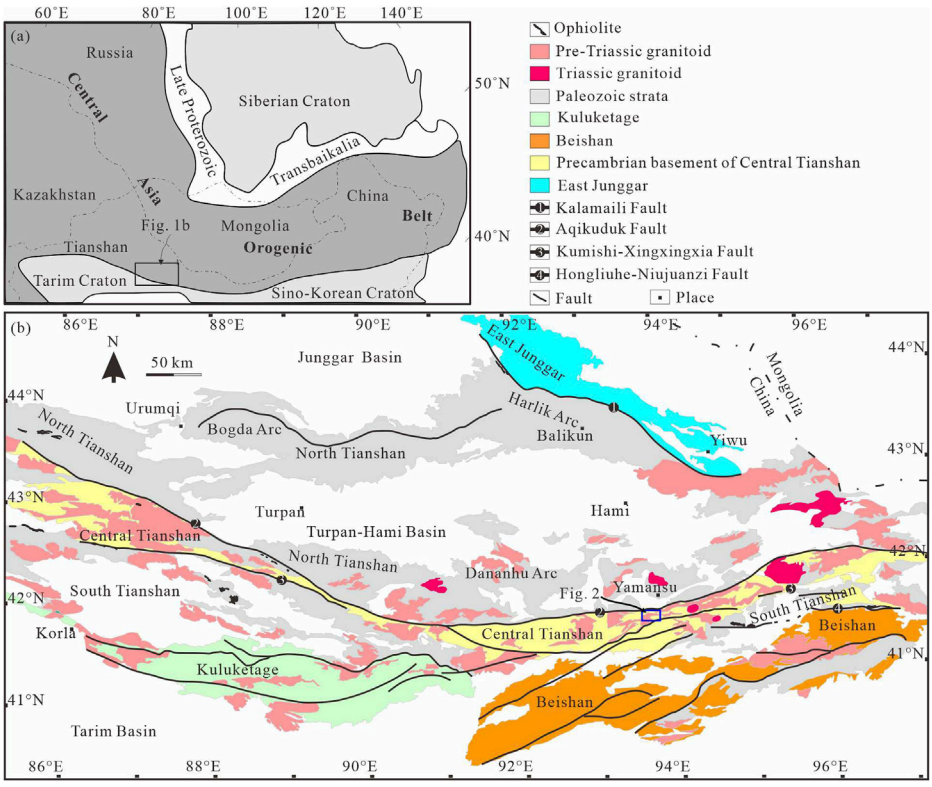

FIGURE 1
(A) Simplified geological map showing the location of Eastern Tianshan relative to the Central Asian Orogenic Belt [modified after Jahn et al. (2000)].
(B) Regional geological map of Eastern Tianshan showing the location of the study area [modified after Zhang et al. (2016a) and Zhi et al. (2021)].

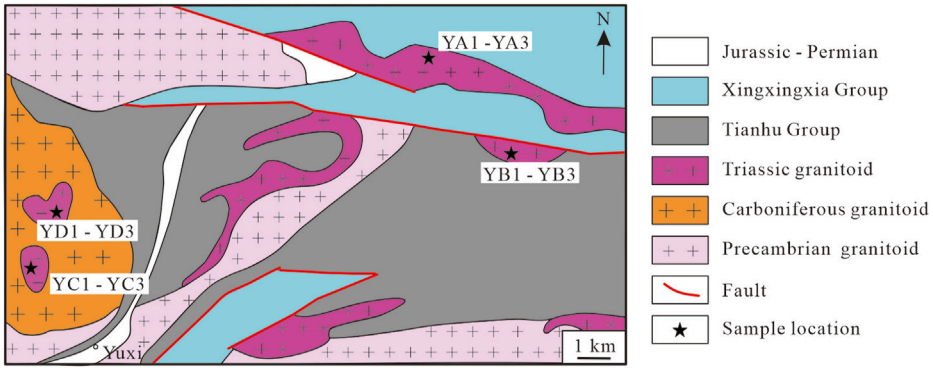

FIGURE 2
Simplified geological map of the study area [modified after BGMRXUAR (2013)].

2 Geological background and sampling

Bounded by the Junggar terranes to the north and the Tarim Block to the south, the Eastern Tianshan occupies the eastern part of the E-W trending Chinese Tianshan Orogenic Belt (Zhang et al., 2016b). From north to south, it can be divided into the North (NTS), Central (CTS), and South (STS) Tianshan orogenic belts, separated by the Aqikuduk and Kumishi–Xingxingxia faults, respectively (Xiao et al., 2004) (Figure 1B).

The NTS is mainly composed of the Early Carboniferous ophiolite belt and Devonian–Carboniferous island arc, including the Bogda–Harlik, Dananhu, Kangguertage, and Yamansu arcs (Han and Zhao, 2018). The arc regions are occupied mainly by Paleozoic sedimentary-volcanic stratas and magmatic intrusions, with an unverified basement (Zhang et al., 2016b; Han and Zhao, 2018). The CTS is characterized by a Precambrian basement, overlain by Paleozoic volcanic-sedimentary successions (Lei et al., 2011; Zhang et al., 2016b; He et al., 2018). The Precambrian basement is mainly composed of Paleoproterozoic–Neoproterozoic schists, gneisses, migmatites, and marbles (Huang et al., 2015; Du et al., 2018; Lei et al., 2021), which have experienced greenschist-to amphibolite-facies metamorphism (Hu et al., 1998). The Paleozoic volcanic-sedimentary stratas are dominated by greenschists, slates, limestones, and volcanic-siliciclastic rocks (Han and Zhao, 2018). The STS is bounded between the CTS and the northern margin of the Tarim Craton. It is composed dominantly of ophiolitic mélanges and Early Paleozoic sedimentary successions that experienced deformation and localized metamorphism (Wang et al., 2014).

A remarkable feature of Eastern Tianshan is the occurrence of multi-stage ultramafic to granitic intrusions, which were most intensive in the Late Paleozoic and became less frequent and scattered in the Triassic (Zhou et al., 2010). The Triassic intrusions are dominated by granitoids with rare mafic rocks, distributed in the Dananhu, Kangguertage, Yamansu arcs and CTS, with U–Pb zircon ages of ca. 250–223 Ma (Wu et al., 2010; Zhou et al., 2010; Lei et al., 2013; Wang et al., 2015b; Deng et al., 2017; Wu et al., 2017; Zhang et al., 2017; Zhao et al., 2017; Chen et al., 2018; Zhao et al., 2018; Muhtar et al., 2020; Lei et al., 2021; Mao et al., 2021; Zhi et al., 2021; Chen et al., 2022). Some of the Triassic granitoids show adakitic features such as Hongshanliang monzogranite (Zhao et al., 2019) and Baishan granite porphyry (Wang et al., 2015b), interpreted as partial melts mainly derived from thickened lower crusts.

This study collected 12 samples from the southern part of the Yamansu area, located about 130 km southeast of the city of Hami, Xinjiang, and proximal to the regional Aqikuduk Fault on the northern margin of CTS belt (Figures 1B, 2). The detailed sample locations are depicted in Figure 2. Samples YA1–YA3 and YB1–YB3 were collected from two granitic plutons located ca. 12 km northeast of the Yuxi Ag deposit (Figure 2). These plutons are surrounded by the Precambrian basement but their contacts were not observed. Samples YC1–YC3 and YD1–YD3 were taken from two small intrusions located ca. 3 km northwest of the deposit (Figure 2). They intrude the Carboniferous granitoids, which, in turn, intrude the Precambrian Tianhu Group (Figure 2).

These samples are undeformed granitoids. Samples YA1–YA3 were medium to fine-grained granodiorites, consisting mainly of plagioclase (30–35 vol.%), K-feldspar (25–30 vol.%), quartz (20–25 vol.%), biotite (8–10 vol.%), and hornblende (5 vol.%) (Figures 3A, E), with accessory amounts of sphene, apatite, and zircon. Samples YB1–YB3 were medium to coarse-grained monzogranites, composed mainly of quartz (25 vol.%), plagioclase (30–35 vol.%), K-feldspar (30–35 vol.%), and biotite (5 vol.%) (Figures 3B, F), with accessory minerals of zircon, apatite, and Fe–Ti oxides. Samples YC1–YC3 and YD1–YD3 were medium to coarse-grained two-mica granites (Figures 3C, D), composed mainly of quartz (30 vol.%), K-feldspar (30–35 vol.%), plagioclase (25–30 vol.%), biotite (5–8 vol.%), and muscovite (3 vol.%) and trace amounts of zircon, apatite, and Fe–Ti oxides as an accessory (Figures 3G, H).

3 Methods

3.1 Zircon U–Pb dating and Hf isotope analysis

Zircons were extracted from samples YA1, YB1, YC1, and YD1 using heavy liquid and magnetic techniques at Langfang Geological Service Ltd., China. Representative zircon crystals were selected under a binocular microscope, mounted in epoxy resin, and finally polished to expose their centers. Cathodoluminescence (CL) imaging of all zircons was conducted

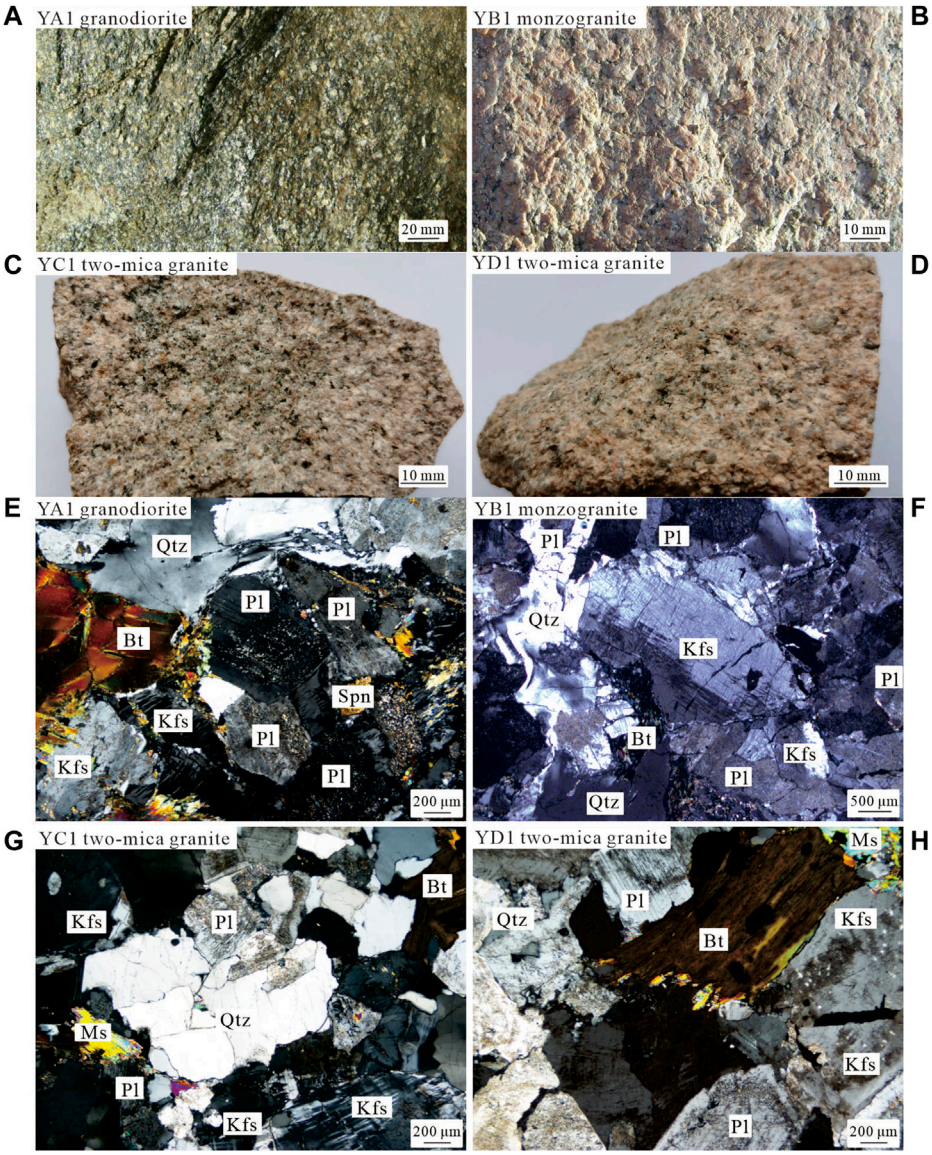

FIGURE 3
Photographs showing the mineralogy and textural features of representative samples of Triassic granitoids in the Yamansu area. Mineral abbreviations: Qtz, quartz; Pl, plagioclase; Kfs, K-feldspar; Bt, biotite; Spn, sphene; Ms, muscovite.

to investigate their internal structures and to guide U–Th–Pb and Lu–Hf isotope analysis. Zircon U–Pb dating was performed using laser ablation multi-collector inductively coupled plasma mass spectrometry (LA-MC-ICP-MS) in the Institute of Mineral Resources, Chinese Academy of Geological Sciences, Beijing. A spot size of 20 μm with a laser ablation rate of 10 Hz was employed for all analyses. The detailed analytical procedure is similar to those reported by Hou et al. (2009). The isotopic ratios were calculated using ICPMSDataCal (Liu et al., 2010), and common Pb correction was made according to Andersen (2002). The concordia diagrams and weighted mean U–Pb ages were obtained using Isoplot (v.3.0) (Ludwig, 2003).

In situ zircon Lu–Hf isotopic analyses were also performed using LA-MC-ICP-MS at the same lab. Analytical spots for Lu–Hf isotopes were located on the previously dated zircon domains or in similar growth domains as inferred from CL images. The detailed analytical method was described by Hou et al. (2007). The analyses were undertaken with a spot diameter of 40 μm, a laser repetition rate of 8 Hz, and a laser energy of 60 mJ. The initial $^{176}Hf/^{177}Hf$ ratios and $\varepsilon_{Hf}(t)$ values were calculated relative to the chondritic reservoir using a $^{176}Hf/^{177}Hf$ ratio of 0.282772 and a $^{176}Lu/^{177}Hf$ ratio of 0.0332 (Blichert-Toft and Albarède, 1997), along with a ^{176}Lu decay constant of 1.865×10^{-11} yr^{-1} (Scherer et al., 2001). Single-stage Hf model ages (T_{DM}) were calculated relative to the depleted mantle with a $^{176}Hf/^{177}Hf$ ratio of 0.279718 at 4.55 Ga and 0.28325 at present, as well as a $^{176}Lu/^{177}Hf$ ratio of 0.0384 (Griffin et al., 2000). Two-stage model ages (T_{DM2}) were calculated using an assumed $^{176}Lu/^{177}Hf$ ratio of 0.015 for the average continental crust (Griffin et al., 2002).

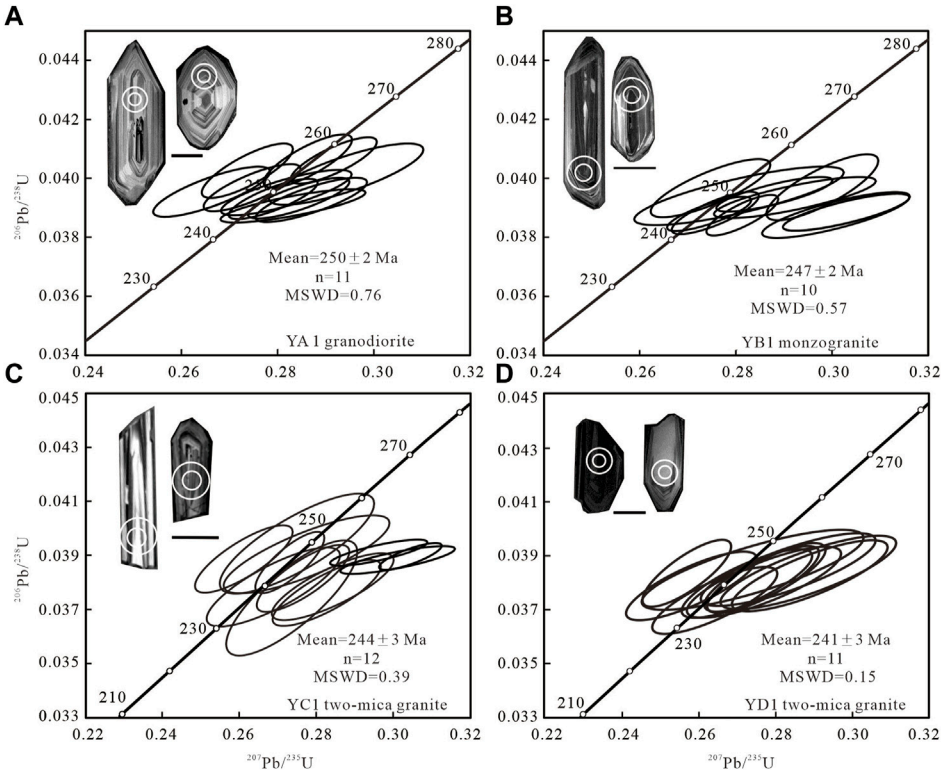

FIGURE 4
Zircon U–Pb concordia diagrams inserted with representative CL images. The smaller line circles show U-Pb dating spots, and the bigger circles show Lu–Hf isotope analysis. Black scale bar is 50 μm.

3.2 Major- and trace-element analysis

Whole-rock major- and trace-element analyses were performed at ALS Chemex Co. Ltd. in Guangzhou, China. For major elements, the prepared samples were first fused with lithium borate flux and then poured into a platinum mold. The resultant disk was then analyzed by X-ray fluorescence spectroscopy. The analytical precision was better than 2%. For trace elements, the prepared samples were added to lithium metaborate flux, mixed well, and fused in a furnace at 1025°C. The resulting melt was then cooled and dissolved in an acid mixture containing nitric, hydrochloric, and hydrofluoric acids. This solution was then analyzed by inductively coupled plasma-mass spectrometry (ICP-MS). The analytical uncertainty is generally <5%.

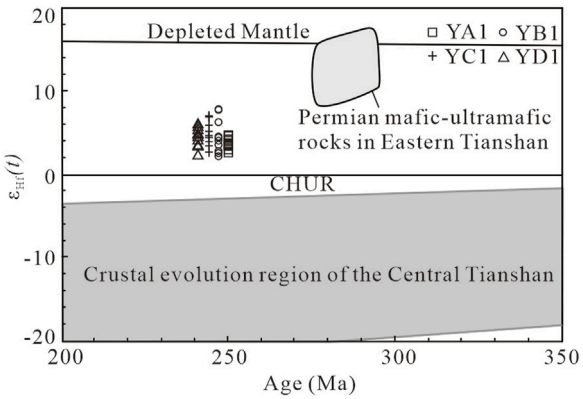

FIGURE 5
Zircon $\varepsilon_{Hf}(t)$ versus age (Ma) diagrams for Triassic granitoids from Eastern Tianshan. The field for Permian mafic-ultramafic rocks in Eastern Tianshan is from Lei et al. (2021) and references therein. The crustal evolution region of the Central Tianshan is from He et al. (2018).

4 Results

4.1 Zircon U–Pb and Lu–Hf results

The LA-MC-ICP-MS zircon U–Pb results are listed in Supplementary Table S1 and plotted on concordia diagrams, inserted by representative zircon CL images (Figure 4). *In situ*, zircon Lu–Hf isotope data are given in Supplementary Table S2 and plotted in Figure 5.

Zircon grains from the granodiorite (YA1), monzogranite (YB1), and two-mica granite (YC1 and YD1) samples were all transparent and had euhedral to subhedral prismatic shapes. They were 60–230 μm in length with length/width ratios of 1:1–4.5:1 and showed oscillatory zoning (Figure 4), indicating magmatic origin (Corfu et al., 2003). Some zircon grains exhibited core-rim structures. All analyzed spots had Th of 45 × 10^{-6}–1067 × 10^{-6}, U of 64 × 10^{-6}, and −2142 × 10^{-6}, with Th/U ratios

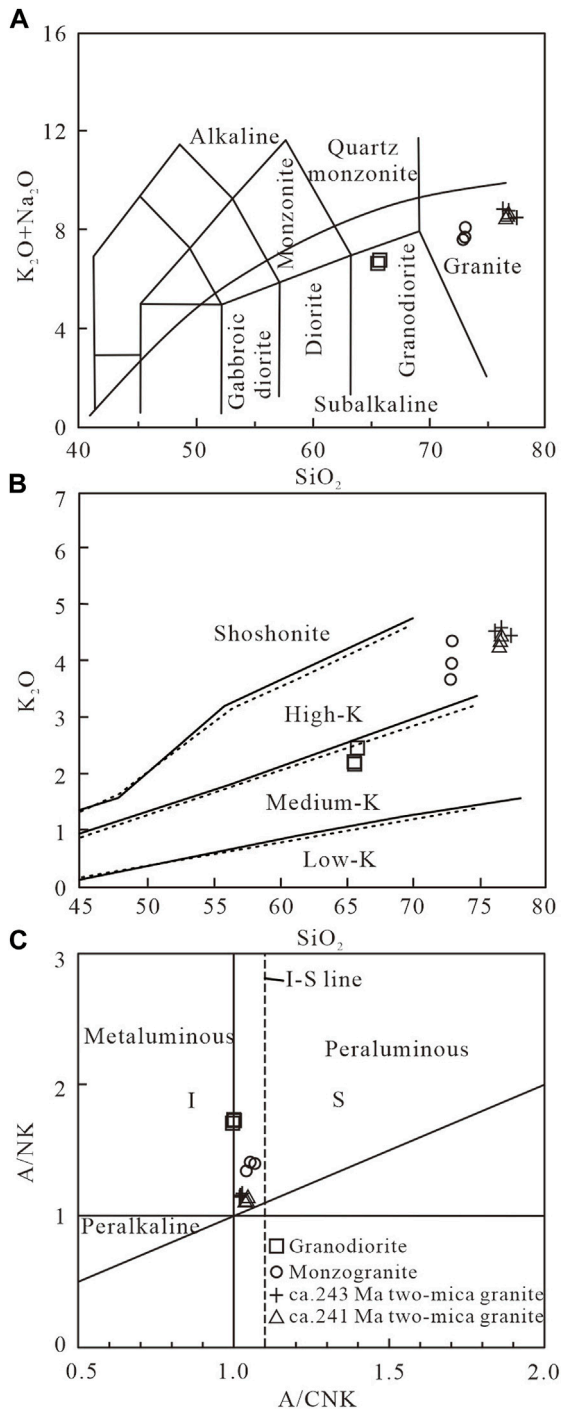

FIGURE 6
(A) $K_2O + Na_2O$ versus SiO_2 diagram [after Le Bas et al. (1986)]. **(B)** K_2O versus SiO_2 diagram [after Peccerillo and Taylor (1976)]. **(C)** A/NK versus A/CNK diagram [after Maniar and Piccoli (1989)]. Major oxides are in wt.% (water-free). A/NK, molar $Al_2O_3/(Na_2O + K_2O)$; A/CNK, molar $Al_2O_3/(CaO + Na_2O + K_2O)$.

of 0.32–1.34. The weighted mean $^{206}Pb/^{238}U$ ages were interpreted as the magma crystallization ages.

Eleven analyses of zircons from sample YA1 yielded $^{206}Pb/^{238}U$ ages of 247 Ma to 257 Ma, giving a concordant population with a weighted mean $^{206}Pb/^{238}U$ age of 250 ± 2 Ma (MSWD = 0.76) (Figure 4A). The Lu–Hf isotopic compositions of the dated ten zircons exhibited positive $\varepsilon_{Hf}(t)$ values of +4.6 to +2.5, with T_{DM2} varying from 1115 Ma to 981 Ma (Figure 5).

Ten analyses of zircons from sample YB1 showed similar apparent $^{206}Pb/^{238}U$ ages ranging from 240 Ma to 251 Ma and yielded a weighted mean $^{206}Pb/^{238}U$ age of 247 ± 2 Ma (MSWD = 0.57) (Figure 4B). All the dated grains were analyzed for their Hf isotopic composition. They had $\varepsilon_{Hf}(t)$ values of +7.8 to +2.2, with T_{DM2} varying from 1133 Ma to 773 Ma (Figure 5).

Twelve analyses on zircons from sample YC1 had $^{206}Pb/^{238}U$ ages ranging from 237 Ma to 250 Ma, forming a tight cluster on a concordia diagram with a weighted mean $^{206}Pb/^{238}U$ age of 244 ± 3 Ma (MSWD = 0.50) (Figure 4C). Eleven spots on the dated grains analyzed for their Hf isotopic composition showed $\varepsilon_{Hf}(t)$ values of +7.0 to +2.7 and T_{DM2} ranging from 1098 Ma to 824 Ma (Figure 5).

Eleven analyses of zircons from sample YD1 had $^{206}Pb/^{238}U$ ages ranging from 236 Ma to 244 Ma, producing a concordant population with a weighted mean $^{206}Pb/^{238}U$ age of 241 ± 3 Ma (MSWD = 0.15) (Figure 4D). Ten dated zircons were analyzed for Hf isotopic composition, producing $\varepsilon_{Hf}(t)$ values of +5.9 to +2.1, corresponding to T_{DM2} values of 1132 Ma to 892 Ma (Figure 5).

Collectively, the zircon U–Pb dating results indicated that the studied granitoids were emplaced in the Early Triassic. The zircon Lu–Hf isotope compositions suggested that their parental magmas were mainly derived from juvenile sources.

4.2 Major and trace elements

The whole-rock major- and trace-element compositions of the Triassic granitoids from Eastern Tianshan are given in Supplementary Table S3 and plotted in Figures 6 and 7. All samples had a low loss on ignition (LOI) values (<0.95) and were not correlated with the mobile element contents (e.g., K, Rb, and Ba, not shown), indicating insignificant alteration.

4.2.1 Granodiorites

The granodiorite samples (YA1–YA3) had SiO_2 contents of 64.62–65.04 wt.%, with Na_2O of 4.33–4.47 wt.%, K_2O of 2.15–2.43 wt.%, and K_2O/Na_2O ratios of 0.48–0.56, belonging to the medium-K calc-alkaline series (Figures 6A, B). Their FeOt and MgO contents ranged from 3.81 to 3.92 wt.% and from 1.63 to 1.69 wt.%, respectively, resulting in $Mg^{\#}$ values of 43–44. The samples had Al_2O_3 contents of 16.59–16.71 wt.% and CaO of 3.79–3.87 wt.%, corresponding to A/CNK ratios of 1.00 (Figure 6C).

The trace element compositions showed lower Cr (59×10^{-6}–69×10^{-6}), and Ni (6.9×10^{-6}–7.2×10^{-6}) concentrations compared to mantle-derived magmas (Baker et al., 1995). They also had high Sr (479×10^{-6}–494×10^{-6}) and low Rb (116×10^{-6}–124×10^{-6}) contents, corresponding to low Rb/Sr ratios (<1). In the trace element spider diagrams (Figure 7A), the granodiorites showed negative Ba, Nb, Ta, Sr, and Ti anomalies. They also had fractionated chondrite-normalized REE patterns ($(La/Yb)_N$ = 14–18) and moderate negative Eu anomalies (Eu/Eu* = 0.56–0.57) (Figure 7B).

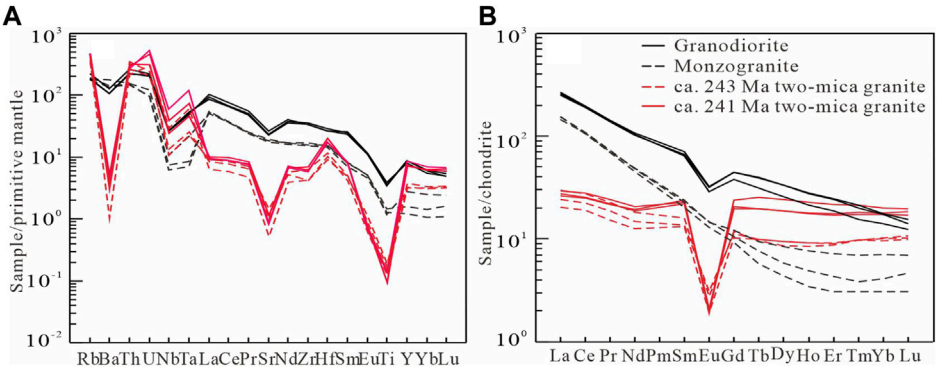

FIGURE 7
(A) Primitive-mantle normalized trace element spider diagrams and **(B)** chondrite-normalized REE patterns. Primitive-mantle, chondrite values from Sun and McDonough (1989).

4.2.2 Monzogranites

Compared with the granodiorites, the monzogranites (samples YB1–YB3) had higher SiO_2 (71.64–71.81 wt.%) and K_2O (3.60–4.27 wt.%) and lower Al_2O_3 (14.17–14.33 wt.%), MgO (0.53–0.60 wt.%), CaO (1.67–1.86 wt.%), and Na_2O (3.61–3.85 wt.%) contents, with higher K_2O/Na_2O ratios of 0.94–1.18. In the plot of K_2O versus SiO_2 (Figure 6B), they fall within the field of the high-K calc-alkaline series. Their A/CNK values ranged from 1.04 to 1.07, indicating that they were weakly peraluminous (Figure 6C).

Trace element data revealed that these monzogranites had Cr contents of 29×10^{-6}–38×10^{-6} and Ni of 1.6×10^{-6}–2.1×10^{-6}. They also had Sr contents of 367×10^{-6}–404×10^{-6}, with Y contents of 5.6×10^{-6}–12.5×10^{-6}, yielding high Sr/Y ratios of 31–66. In the trace element spider diagrams (Figure 7A), they showed enrichment of large ion lithophile elements (LILE) (e.g., Rb, Ba, Th, and U) and depletion of Nb, Ta, and Ti. The chondrite-normalized REE patterns showed heavy REE depletion with high $(La/Yb)_N$ ratios (21–50) and slightly negative Eu anomalies (Eu/Eu* = 0.80–0.89) (Figure 7B).

4.2.3 Two-mica granites

The ca. 244 Ma and ca. 241 Ma two-mica granites (samples YC1–YC3 and YD1–YD3) had similar whole rock geochemical compositions. Compared to the aforementioned samples, they exhibited higher SiO_2 (75.58–76.78 wt.%), Na_2O (3.93–4.26 wt.%), and K_2O (4.28–4.50 wt%) and lower TiO_2 (0.02–0.04 wt.%), FeOt (0.77–0.83 wt.%), MgO (0.01–0.07 wt.%), and CaO (0.51–0.75 wt.%). They showed high-K calc-alkaline affinity (Figure 6B) and weakly peraluminous character (A/CNK = 1.01–1.05) (Figure 6C).

The trace element compositions showed strong enrichments of Rb, Th, and U, and significant depletions of Ba, Sr, and Ti (Figure 7A). The concentrations of high field strength elements (HFSE, e.g., Nb, Ta, and Zr) were low (e.g., $Zr = 47 \times 10^{-6}$–78×10^{-6}). They also had high Y/Ho (30–34) and low Zr/Hf (12–20), Nb/Ta (<10), and K/Rb (122–154) ratios, significantly different from the chondrite values (Y/Ho = 28, Zr/Hf = 36, Nb/Ta = 18, and K/Rb = 235, (Sun and McDonough, 1989)). Additionally, they displayed flat chondrite-normalized REE patterns ($(La/Yb)_N$ = 1.30–2.90) with pronounced negative Eu anomalies (Eu/Eu* = 0.08–0.25) (Figure 7B) and REE contents (35×10^{-6}–58×10^{-6}) obviously lower than the average value of granite worldwide (288×10^{-6}) (Wu et al., 2015).

5 Discussion

5.1 Petrogenesis

5.1.1 Granodiorites

The granodiorites had higher SiO_2 (64.62–65.04 wt.%) and lower $Mg^{\#}$ (43–44), Cr (59×10^{-6}–69×10^{-6}), and Ni (6.9×10^{-6}–7.2×10^{-6}) contents compared to mantle-derived magmas (Baker et al., 1995), excluding an M-type origin. Furthermore, the absence of typical Al-rich minerals (e.g., cordierite and garnet) in the samples, in combination with their high Na_2O (>4.3 wt.%), CaO/FeOt (>0.98) but low Rb/Ba (0.15–0.16) and Rb/Sr (0.24–0.25) values, excluded them as S-type granitoids (Zhang et al., 2017). In addition, samples YA1–YA3 contained amphibole and biotite (not a late crystallizing phase, Figure 3E) but lacked pyroxene or fayalite, and had relatively low $Na_2O + K_2O$ (6.72–6.85 wt.%), Nb (16.8×10^{-6}–19.1×10^{-6}), Y (32.0×10^{-6}–40.1×10^{-6}), Ga (26×10^{-6}), and Zn (88×10^{-6}–91×10^{-6}) contents and FeOt/MgO (2.28–2.34), K_2O/MgO (1.28–1.49) values, distinguishing them from A-type suite (Whalen et al., 1987). Finally, these samples contained hornblende and biotite, and plotted in the I-type granitoid field in the A/NK versus A/CNK (Figure 6C), suggestive of I-type affinities.

Calc-alkaline I-type granitoids are commonly generated by 1) partial melting of lower crustal rocks (Griffin et al., 2002; Ju et al., 2017); 2) mixing of mantle-derived basaltic magma with crustal derived felsic magma (Barbarin, 1999; Zhu et al., 2009); and 3) melting of a subducted oceanic crust. First, mafic xenoliths/enclaves have not been found in the intrusion from which the granodiorites (YA1–3) were sampled. Such a characteristic does not favor the mixing of the mantle- and crust-derived components. Second, zircons from the granodiorite had a narrow range of Hf isotopic compositions ($\varepsilon_{Hf}(t)$ = +4.6–+2.5, Figure 5), which is atypical for

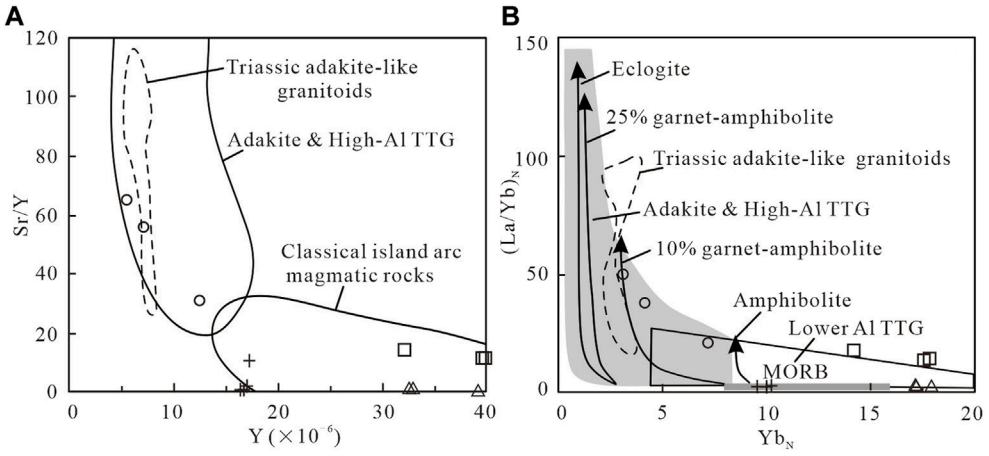

FIGURE 8
Discrimination diagrams for adakitic rocks. **(A)** Sr/Y versus Y diagram (Atherton and Petford, 1993); **(B)** $(La/Yb)_N$ versus Yb_N diagram (Defant and Drummond, 1990). The symbols are the same as in Figure 6. The fields for Triassic adakite-like granitoids are from Zhang et al. (2015) and Zhao et al. (2019).

magmas incorporating both mantle- and crustal-derived melts. Moreover, the granodiorites showed low MgO contents (3.81–3.92 wt.%) and $Mg^{\#}$ values (43–44), in contrast to the magmas directly derived from the partial melting of subducted oceanic crustal rocks that typically have high $Mg^{\#}$ values (>50) (Rapp et al., 1999; Guan et al., 2012). Thus, we inferred that the partial melting of continental crust played a significant role in the generation of these granitoids. This interpretation is supported by the whole-rock trace element ratios, such as Ti/Zr (14.9–17.9), Ti/Y (149.5–187.3), and Nb/Ta (8.5–9.5) values that are comparable with those (Ti/Zr < 30, Ti/Y < 200, and Nb/Ta = 12) of continental crustal rocks (Rudnick and Fountain, 1995). They also showed low Sr/Y ratios (12–15), moderately negative Eu anomalies (Eu/Eu^{*} = 0.56–0.57), and relatively high HREE contents (e.g., Yb = 2.41 × 10^{-6}–3.03 × 10^{-6}), implying partial melting under the plagioclase stability condition with little or no garnet (corresponding to pressures <12 kbar) (Luo et al., 2012; Wang et al., 2016). In addition, the granodiorites exhibited $\varepsilon_{Hf}(t)$ values of +4.6 to +2.5, plotting below the depleted mantle evolution line and the composition of typical Permian mantle-derived mafic-ultramafic rocks in the region (Lei et al., 2021), but above the crustal evolution region of the Central Tianshan (He et al., 2018) (Figure 5). Their Hf two-stage model ages of 1115 Ma to 981 Ma are significantly younger than those of the Central Tianshan metamorphic basement rocks (He et al., 2018). These features suggest that the juvenile material played a key part in the granodiorite formation. We, therefore, concluded that the studied granodiorites were most probably derived from the partial melting of juvenile crustal materials with plagioclase as a major residual phase at pressures <12 kbar.

5.1.2 Monzogranites

The monzogranites showed low Y (5.6 × 10^{-6}–12.5 × 10^{-6}) and HREE (e.g., Yb = 0.53 × 10^{-6}–1.22 × 10^{-6}) contents and high Sr/Y (31–66) and $(La/Yb)_N$ (21–50) ratios, consistent with adakite-like rocks (Figure 8). This feature is similar to Triassic adakite-like granitoids in the region (Figure 8), indicating their petrogenetic analogy. Several genetic models have been proposed for the origin of adakitic rocks, including: 1) crustal assimilation and fractional crystallization (AFC) processes of basaltic magma (Castillo et al., 1999); 2) partial melting of subducted oceanic slab (Defant and Drummond, 1990); and 3) partial melting of thickened (Chung et al., 2003; Long et al., 2015) or delaminated mafic lower crust (Gao et al., 2004).

Generally, AFC processes of basaltic magma necessitate significant volumes of mafic melts (Castillo et al., 1999; Castillo, 2006), and the resultant adakitic rocks typically contain mafic minerals (e.g., amphibole and clinopyroxene) (Zhang et al., 2016a). The absence of amphibole and clinopyroxene in the samples, together with the lack of voluminous coeval mafic rocks in the study area, does not support an origin from basaltic magma by AFC processes. Moreover, the monzogranites showed relatively large variations in Sr/Y (31–66), $(La/Yb)_N$ (21–50), Zr/Nb (23–38), and Nb/Ta (8.8–15.2) ratios at similar SiO_2 contents, precluding fractionation processes (Zhang et al., 2016a).

Adakitic rocks generated by the partial melting of subducted oceanic slab or delaminated lower crust generally have high $Mg^{\#}$ (≥42), Cr (≥36 × 10^{-6}), and Ni (≥24 × 10^{-6}) values due to melt-mantle interactions during magma ascent (Martin, 1999; Gao et al., 2004). However, the studied monzogranites had low $Mg^{\#}$ (34), Cr (29 × 10^{-6}–38 × 10^{-6}), and Ni (1.6 × 10^{-6}–2.1 × 10^{-6}) values. In addition, they had Rb/Sr ratios of 0.30–0.31, higher than those (<0.05) of slab-derived adakitic rocks (Huang et al., 2009). Moreover, lithospheric delamination typically results in mafic magmatism that transitioned from "older" lithospheric mantle to "young" asthenospheric mantle over tens of millions of years (Ducea, 2011), which has not been documented in the CTS during the Triassic. Thus, the studied monzogranites were unlikely to have resulted from the partial melting of the oceanic slab or delaminated lower crust.

The monzogranites had high SiO_2 and low MgO, $Mg^{\#}$, Ni, and Cr values, with $\varepsilon_{Hf}(t)$ values of +7.8 to +2.2 and corresponding T_{DM2}

of 1133–773 Ma, indicating that their parental magma derived from thickened juvenile lower crust, consistent with the petrogenesis of Triassic adakite-like granitoids previously reported in the region (Zhang et al., 2015; Zhao et al., 2019). In addition, the relatively high Sr/Y and $(La/Yb)_N$ ratios of the monzogranites indicated the pluton formation in the stability field of garnet with little or no plagioclase; i.e., pressures >12 kbar (Wang et al., 2016). However, the relatively low Nb/Ta ratios (9–15) imply a rutile-free source. Therefore, the depth of partial melting for the monzogranites was constrained to 12–15 kbar, indicating a crustal source dominated by garnet amphibolite (Yuan et al., 2010).

5.1.3 Two-mica granites

The ca. 244 Ma and ca. 241 Ma two-mica granites had approximately coeval ages within error. Furthermore, they displayed similar REE distribution patterns and primitive mantle-normalized spider diagrams (Figure 7), together with similar $\varepsilon_{Hf}(t)$ values (Figure 5), indicating similar geochemical affinities and magma sources. Compared with relatively unfractionated granitoids in the area, they contained higher concentrations of SiO_2, Na_2O, and K_2O, and lower concentrations of FeOt, MgO, and CaO, with more significant Rb, Th, and U enrichment and Ba, Sr, Eu, and Ti depletion (Figure 7A). In addition, their differentiation indicators, such as the Y/Ho (30–34), Zr/Hf (12–20), Nb/Ta (<10), and K/Rb (122–154) ratios, significantly deviated from those of chondrite (Y/Ho = 28, Zr/Hf = 36, Nb/Ta = 18, and K/Rb = 235; Sun and McDonough, 1989). These observations demonstrated that the Triassic two-mica granites were highly fractionated granites.

The alkaline mineral was absent in the two-mica granites studied, with the presence of subhedral biotite crystals rather than interstitial biotite. In combination with the low REE, Y, Zr, and Zn contents, it is reasonable to infer that these two-mica granites are not A-type granites (Whalen et al., 1987). In addition, they were weakly peraluminous (A/CNK <1.1, Figure 6C), with low P_2O_5 (0.01%) contents and normative corundum (<1%), similar to the diagnostic features of I-type rather than S-type granites (Chappell and White, 2001). Thus, we concluded that these two-mica granites were highly fractionated I-type granites.

It is generally agreed that highly fractionated I-type granite is formed by 1) complete fractional crystallization of mantle-derived mafic magmas (Wyborn et al., 2001) or 2) partial melting of crustal materials, accompanied by subsequent fractional crystallization (Ju et al., 2017; Liao et al., 2019). For the studied two-mica granites, the latter mechanism may be more reasonable, as the requisite voluminous mafic rocks to be parental materials were not observed in the study area. Furthermore, their zircon $\varepsilon_{Hf}(t)$ values ranged from +7.0 to +2.1, with Hf model ages (T_{DM2}) of 1132 Ma to 824 Ma, indicating that the parental magma derived from isotopically juvenile crustal materials. The crustal materials should be medium-to-high-K mafic to intermediate rocks, as inferred from their high-K calc-alkaline I-type affinity, with $K_2O/Na_2O > 1$ (Roberts and Clemens, 1993; Sisson et al., 2005). The flat HREE patterns of these two-mica granites suggest the absence of residual garnet during partial melting. As the lower limit of garnet stability is 5 kbar (Wang et al., 2016), the studied two-mica granites were likely generated by the partial melting of crustal rocks in the pressure range of ≤5 kbar. The subsequent fractional crystallization process was dominated by feldspar, as deduced from the high Rb contents (240×10^{-6}–301×10^{-6}) and Rb/Sr ratios (8.63–21.92), as well as the significant negative Eu anomalies (Figure 7B) (Ju et al., 2017). Therefore, the two-mica granites were formed by the partial melting of juvenile crustal materials accompanied mainly by fractional crystallization of feldspar before the final emplacement.

5.2 Triassic magmatism in Eastern Tianshan

Triassic plutons have been reported in Eastern Tianshan, such as ca. 253–246 Ma granitoids and ca. 251–247 Ma gabbros in the Jingerquan region (Liu et al., 2020), ca.250 Ma Baishitouquan pluton (Zhi et al., 2021), ca. 250–235 Ma Hongshanliang granitoids (Zhao et al., 2019), ca. 251–241 Ma Tianhu pluton (Lei et al., 2013; Zhao et al., 2017; Lei et al., 2021), ca. 249–240 Ma Guobaoshan amazonite granite (Chen et al., 2022), ca. 246–230 Ma Weiya magmatic complex (Zhang et al., 2005; Wu et al., 2010; Feng and Zheng, 2021), ca. 246 Ma Tudun K-feldspar granite (Zhou et al., 2010), ca. 246–240 Ma Xiaobaishitou biotite granite (Deng et al., 2017; Li et al., 2019), ca. 239 Ma Houshan granite (Lei et al., 2013) and Shadong concealed granite (Chen et al., 2018), ca. 237–231 Ma Donggebi porphyritic granite (Sun et al., 2017; Wu et al., 2017), ca. 236–228 Ma Bailingshanxi gabbro and porphyritic granite (Gao et al., 2021), ca. 230–222 Ma Yamansubei pluton (Lei et al., 2013; Zhang et al., 2017; Zhao et al., 2018), and ca. 228–226 Ma Baishan granite porphyry (Zhang et al., 2015; Wang et al., 2015b; Wang et al., 2016).

The zircons from the granitoid samples in this study, characterized by euhedral to subhedral shapes, oscillatory zoning structures, and relatively high Th/U ratios (0.31–1.34), yielded weighted mean $^{206}Pb/^{238}U$ ages of 250–241 Ma, representing the crystallization ages of the granitoids. These dating results in conjunction with the aforementioned geochronological data indicate significant Triassic magmatism in Eastern Tianshan; thus, the Triassic period is an important magmatism epoch in Eastern Tianshan. Moreover, several Triassic granitoids were also identified in the adjacent Beishan area (Li et al., 2012), suggesting that the Eastern Tianshan may have been connected to the Beishan area during the Triassic and, thus, they may have been controlled by the same geodynamic regime at that time.

5.3 Tectonic implications

Recent results from detrital zircons provenance analyses (Zhang et al., 2016c), paleomagnetic research (Wang et al., 2007), and structural analyses (Wang et al., 2014) suggested closure of the Paleo-Asian Ocean most likely in the Late Carboniferous to the Early Permian and post-collisional environment since the earliest Permian in Eastern Tianshan. The Permian post-collisional environment is also evidenced by the occurrence of the Early Permian A_2 type felsic magmatism (Zhou et al., 2010; Chen et al., 2011) and ca. 295–265 Ma bimodal magmatic suites constituted by mafic-ultramafic intrusive complexes and undeformed granitic distributed in the North Tianshan (Han and Zhao, 2018). Furthermore, it is generally accepted that post-collisional magmatism signifies the end of the orogenic cycle,

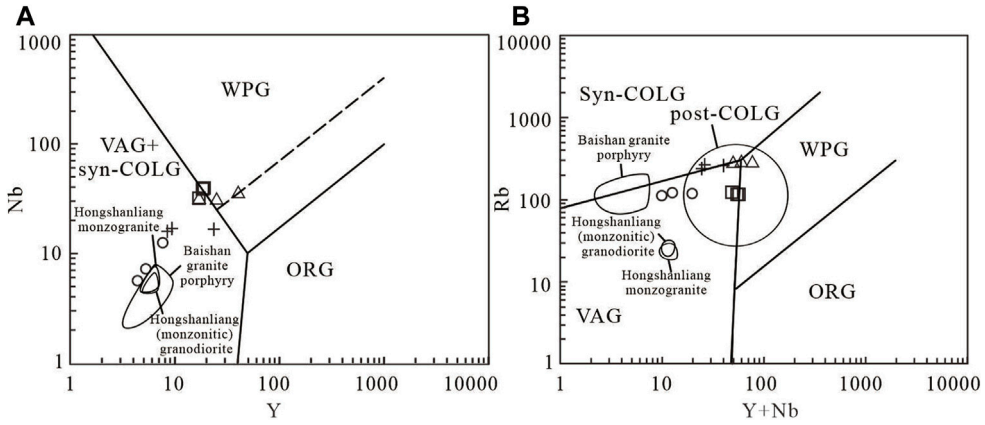

FIGURE 9
Discrimination diagrams of Triassic granitoids in Eastern Tianshan (Pearce et al., 1984). **(A)** Nb versus Y diagram; **(B)** Rb versus Y + Nb diagram; ORG, ocean ridge granite; WPG, within plate granite; VAG, volcanic arc granite; syn-COLG, syn-collisional granite; post-COLG, post-collisional granite. The symbols are the same as in Figure 6. The fields for Triassic adakite-like granitoids (Baishan granite porphyry, Hongshanliang (monzonitic) granodiorite, and monzogranite) are from Zhang et al. (2015) and Zhao et al. (2019).

with a duration of ~10–40 Ma (Song et al., 2015). Thus, it is reasonable that the subsequent intracontinental environment commenced at the latest in the Early Triassic.

Meanwhile, the Triassic magmatism of Eastern Tianshan shows features including a) sporadic occurrence of small granitic intrusions, with predominantly nearly elliptical shape (Figure 2; Zhou et al., 2010; Mao et al., 2015), b) a regional distribution (Wu et al., 2010), c) rare mafic magmatism, except for the Weiya gabbro (Zhang et al., 2005; Zhang et al., 2007) and coeval mafic dykes (Wang et al., 2008), and d) the presence of highly fractionated I-type granites. These differ obviously from those of voluminous Permian magmatism characterized by abundant A-type granitoids and coeval voluminous mafic-ultramafic intrusions, exhibiting orogen-parallel distributions (Han and Zhao, 2018). This contrast indicates a diminished impact of the continental collision related to the Paleo-Asian Ocean tectonic evolution on Eastern Tianshan during the Permian, and that the Triassic magmatism was mainly controlled by a different tectonic regime. The magmatism of the Triassic granitoids occurred synchronous with a series of geological events resulting from the progressive closure of the Paleo-Tethys Ocean (such as rotations of the Junggar Block, ductile shearing of the Xingxingxia Fault, and exhumation of the Beishan Terrane) (Wang et al., 2010; Choulet et al., 2013; Gillespie et al., 2017). Therefore, the closure of the Paleo-Tethys may have provided a dynamic trigger for the Triassic magmatism in Eastern Tianshan (Wu et al., 2010; Zhang et al., 2017; Feng and Zheng, 2021).

The adakite-like rocks, including ca. 247 Ma monzogranites presented here and ca. 250 Ma Hongshanliang (monzonitic) granodiorite (Zhao et al., 2019), were mostly plotted in the fields of VAG + syn-COLG (Figure 9) (Pearce et al., 1984), suggesting a compressional environment during the Early Triassic (Zhang et al., 2015) in Eastern Tianshan. Similarly, the ca. 235 Ma Hongshanliang monzogranite (Zhao et al., 2019) and ca. 228 Ma Baishan granite porphyry (Zhang et al., 2015), mainly derived from thickened lower crust, also plotted in the VAG + syn-COLG fields (Figure 9), suggesting a compressional environment during the early Late Triassic. In combination with a series of compressional tectonic events in the adjacent regions, including a) counter-clockwise rotations of the Junggar relative to the Tarim between the Early and the Late Triassic (Choulet et al., 2013), and b) exhumation of the Beishan terrane initiated at ~230 Ma (Gillespie et al., 2017), it is reasonable to propose that Eastern Tianshan was in a continuous compressional setting in the Early Triassic to the early Late Triassic.

By contrast, the (highly fractionated) I-type granitoids in this study mainly fell within the post-COLG field in Figure 9B, suggesting an extensional environment. However, the tectonic discrimination diagrams for granitoids were not convincing, especially for those highly fractionated I-type granitoids. Therefore, this evidence is less robust. Nonetheless, a Triassic extensional setting has often been proposed as a possible tectonic regime in Eastern Tianshan. This inference is supported by the presence of a 246–230 Ma Weiya intrusive complex (Zhang et al., 2005; Wu et al., 2010; Feng and Zheng, 2021), 234–231 Ma Donggebi granitoids with A-type features (Li et al., 2012; Sun et al., 2017), and 222 Ma Tianhu lamprophyre dykes and coeval Hongliuhe diabase dykes (Wang et al., 2008) in Eastern Tianshan and adjacent Beishan area. Furthermore, the extensional setting is reinforced by the observations that several mineral deposits (such as the Xiaobaishitou deposit formed during the Early Triassic (Li et al., 2019) and the Donggebi deposit formed in the Early to Middle Triassic (Sun et al., 2017)) in Eastern Tianshan are associated with a regional extension.

The aforementioned discussion indicates that the compressional and extensional tectonic regimes occurred contemporaneously from the Early Triassic to the Early Late Triassic in Eastern Tianshan. We speculate that the contrasting and contemporaneous tectonic regimes (i.e., compression and extension) occurred at deep and shallower lithosphere depths, respectively. The compressional depth was constrained to >40 km. This is inferred from the petrogenesis of adakite-like granitoids, including monzogranites in this study, Hongshanliang monzogranite (Zhao et al., 2019), and Baishan granite porphyry (Zhang et al., 2015), which were mainly derived

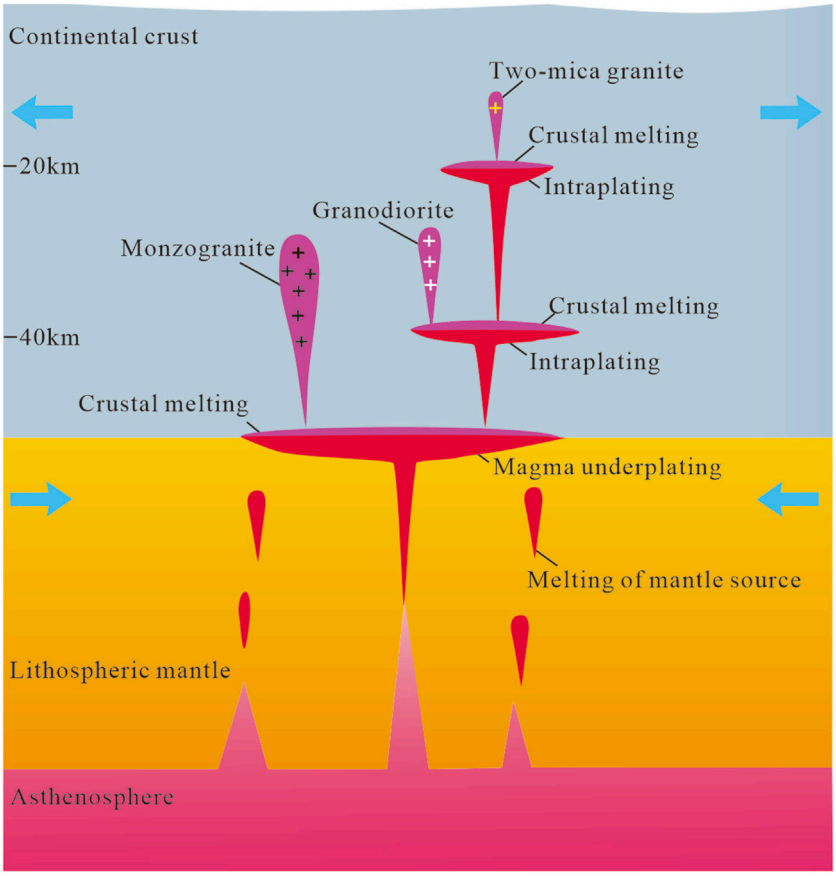

FIGURE 10
Schematic diagram showing granitoid generation in the Yamansu area, Eastern Tianshan.

from a thickened lower crust and formed in a compressional setting. Meanwhile, the extension was inferred to occur at a depth <40 km, based on the petrogenesis of the (highly fractionated) I-type granitoids in this study and the Weiya intrusive complex generated in the pressure range of ≤12 kbar, pointing to an extensional setting (Feng and Zheng, 2021). Such a model involving coeval extension and contraction at different depths is usually attributed to lithosphere flexure, a tectonic scenario commonly noted along convergent margins (Bradley and Kidd, 1991; Davis et al., 1994; Yuan et al., 2010).

Considering the geological evidence described previously, we suggest that the Triassic granitoids in the Yamansu area were generated in an intracontinental environment. In Eastern Tianshan, contemporaneous compression and extension existed at deep and shallower lithosphere depths, respectively, during the Triassic (Figure 10). In the deep lithosphere, some fractures must have formed within the compressional lithospheric mantle and provided channels for upwelling asthenospheric mantle (Figure 10). This upwelling elevated the geotherm, providing the necessary heat for the partial melting of the lithospheric mantle. Underplating of the mantle-derived magmas at the deep crust could promote the partial melting of the thickened lower crust to generate the adakite-like monzogranitc magma. Later, the intraplating of these mantle-derived magmas at the middle to the lower crust could have promoted the partial melting of the corresponding crustal sources to produce the granodioritic and granitic magmas.

6 Conclusion

Based on new whole-rock geochemical compositions, as well as LA-MC-ICP-MS U–Pb zircon dating and Hf isotopic analyses of granitoids in Eastern Tianshan, the following conclusions can be drawn:

(1) Triassic granitic magmatism, represented by intrusions of granodiorite, monzogranite, and two-mica granite in the Yamansu area on the northern margin of the CTS belt, yield zircon U–Pb ages of ca. 250–241 Ma. Combined with previous geochronology studies, we suggest significant Triassic magmatism in Eastern Tianshan; thus, the Triassic period was an important magmatism epoch in Eastern Tianshan.
(2) The granitoids were formed by the partial melting of juvenile materials at various crustal levels in the region. The granodiorites (ca. 250 Ma) were calc-alkaline I-type granites derived from the partial melting of juvenile crustal materials at pressures <12 kbar. The monzogranites (ca. 247 Ma) were adakitic and were formed by partial melting of the thickened

lower crust at relatively high pressures (12–15 kbar). The two-mica granites (ca. 244 Ma and ca. 241 Ma) were highly fractionated I-type granites generated by the melting of medium-to high-K mafic to intermediate crustal rocks at pressures <5 kbar, accompanied mainly by subsequent fractional feldspar crystallization.

(3) The granitoids were formed in an intracontinental environment, possibly controlled mainly by the far-field effects of the Paleo-Tethys system.

(4) In Eastern Tianshan, contemporaneous compression and extension existed at deep and shallower lithosphere depths, respectively, during the Triassic.

Data availability statement

The original contributions presented in the study are included in the article/Supplementary Material. Further inquiries can be directed to the corresponding author.

Author contributions

HC provided initial data and wrote the paper. KW designed the study. XG conducted the fieldwork. GL participated in petrology and photomicrograph analyses. RG assisted with the LA-ICP-MS zircon U–Pb dating and Hf isotopic analysis.

Funding

This research was financially supported by the Natural Science Foundation (No. 2021D01C040) and Universities Research Program (No. XJEDU2020Y005) of the Xinjiang Uygur Autonomous Region of China, the National Natural Science Foundation of China (No. U1403291), and the China Postdoctoral Science Foundation (No. 2017M613257).

Acknowledgments

The authors are very grateful to the reviewers for their constructive comments and insightful suggestions for improving the manuscript.

Conflict of interest

The authors declare that the research was conducted in the absence of any commercial or financial relationships that could be construed as a potential conflict of interest.

Publisher's note

All claims expressed in this article are solely those of the authors and do not necessarily represent those of their affiliated organizations, or those of the publisher, the editors, and the reviewers. Any product that may be evaluated in this article, or claim that may be made by its manufacturer, is not guaranteed or endorsed by the publisher.

Supplementary material

The Supplementary Material for this article can be found online at: https://www.frontiersin.org/articles/10.3389/feart.2023.1164162/full#supplementary-material

References

Andersen, T. (2002). Correction of common lead in U-Pb analyses that do not report ^{204}Pb. *Chem. Geol.* 192, 59–79. doi:10.1016/S0009-2541(02)00195-X

Atherton, M. P., and Petford, N. (1993). Generation of sodium-rich magmas from newly underplated basaltic crust. *Nature* 362, 144–146. doi:10.1038/362144a0

Baker, M. B., Hirschmann, M. M., Ghiorso, M. S., and Stolper, E. M. (1995). Compositions of near-solidus peridotite melts from experiments and thermodynamic calculations. *Nature* 375, 308–311. doi:10.1038/375308a0

Barbarin, B. (1999). A review of the relationships between granitoid types, their origins and their geodynamic environments. *lithos* 46, 605–626. doi:10.1016/S0024-4937(98)00085-1

BGMRXUAR (Bureau of Geology and Mineral Resources of Xinjiang Uygur Autonomous Region) (2013). Geological report for 1:250000 suvery of Yamansu area. Report (K46C003003).

Blichert-Toft, J., and Albarède, F. (1997). The Lu-Hf isotope geochemistry of chondrites and the evolution of the mantle-crust system. *Earth Planet. Sci. Lett.* 148, 243–258. doi:10.1016/S0012-821X(97)00040-X

Bradley, D. C., and Kidd, W. S. F. (1991). Flexural extension of the upper continental crust in collisional foredeeps. *Geol. Soc. Am. Bull.* 103, 1416–1438. doi:10.1130/0016-7606(1991)103<1416:FEOTUC>2.3.CO;2

Castillo, P. R. (2006). An overview of adakite petrogenesis. *Chin. Sci. Bull.* 51, 257–268. doi:10.1007/s11434-006-0257-7

Castillo, P. R., Janney, P. E., and Solidum, R. U. (1999). Petrology and geochemistry of camiguin island, southern Philippines: Insights to the source of adakites and other lavas in a complex arc setting. *Contrib. Mineral. Pet.* 134, 33–51. doi:10.1007/s004100050467

Chappell, B. W., and White, A. J. R. (2001). Two contrasting granite types: 25 years later. *Aust. J. Earth Sci.* 48, 489–499. doi:10.1046/j.1440-0952.2001.00882.x

Chen, B. Y., Wu, C. Z., Brzozowski, M. J., Lei, R. X., Muhtar, M. N., Li, T. G., et al. (2022). Geochronology and tectonic setting of the giant Guobaoshan Rb deposit, Central Tianshan, NW China. *Ore Geol. Rev.* 141, 104636. doi:10.1016/j.oregeorev.2021.104636

Chen, C., Lu, X. B., Wu, C. M., Jiang, X., and Mao, C. (2018). Origin and geodynamic implications of concealed granite in Shadong tungsten deposit, Xinjiang, China: Zircon U-Pb chronology, geochemistry, and Sr-Nd-Hf isotope constraint. *J. Earth Sci.* 29, 114–129. doi:10.1007/s12583-017-0808-7

Chen, X. J., Shu, L. S., and Santosh, M. (2011). Late Paleozoic post-collisional magmatism in the Eastern Tianshan Belt, Northwest China: New insights from geochemistry, geochronology and petrology of bimodal volcanic rocks. *lithos* 127, 581–598. doi:10.1016/j.lithos.2011.06.008

Choulet, F., Chen, Y., Cogné, J. P., Rabillard, A., Wang, B., Lin, W., et al. (2013). First triassic palaeomagnetic constraints from junggar (NW China) and their implications for the mesozoic tectonics in central asia. *J. Asian Earth Sci.* 78, 371–394. doi:10.1016/j.jseaes.2013.01.023

Chung, S. L., Liu, D. Y., Ji, J. Q., Chu, M. F., Lee, H. Y., Wen, D. J., et al. (2003). Adakites from continental collision zones: Melting of thickened lower crust beneath southern tibet. *geology* 31, 1021–1024. doi:10.1130/G19796.1

Corfu, F., Hanchar, J. M., Hoskin, P., and Kinny, P. (2003). Atlas of zircon textures. *Rev. Mineralogy Geochem.* 53, 469–500. doi:10.2113/0530469

Davis, M. J., Farber, D. L., Wooden, J. L., and Anderson, J. L. (1994). Conflicting tectonics? Contraction and extension at middle and upper crustal levels along the cordilleran late jurassic arc, southeastern California. *geology* 22, 247–250. doi:10.1130/0091-7613(1994)022<0247:ctcaea>2.3.co;2

Defant, M. J., and Drummond, M. S. (1990). Derivation of some modern arc magmas by melting of young subducted lithosphere. *Nature* 347, 662–665. doi:10.1038/347662a0

Deng, X. H., Chen, Y. J., Santosh, M., Wang, J. B., Li, C., Yue, S. W., et al. (2017). U-Pb zircon, Re-Os molybdenite geochronology and Rb-Sr geochemistry from the Xiaobaishitou W (-Mo) deposit: Implications for Triassic tectonic setting in eastern Tianshan, NW China. *Ore Geol. Rev.* 80, 332–351. doi:10.1016/j.oregeorev.2016.05.013

Dong, Y. P., Zhang, G. W., Neubauer, F., Liu, X. M., Hauzenberger, C., Zhou, D. W., et al. (2011). Syn- and post-collisional granitoids in the Central Tianshan orogen: Geochemistry, geochronology and implications for tectonic evolution. *Gondwana Res.* 20, 568–581. doi:10.1016/j.gr.2011.01.013

Du, L., Long, X. P., Yuan, C., Zhang, Y. Y., Huang, Z., Wang, X., et al. (2018). Mantle contribution and tectonic transition in the aqishan-yamansu belt, eastern tianshan, NW China: Insights from geochronology and geochemistry of early carboniferous to early permian felsic intrusions. *lithos* 304-307, 230–244. doi:10.1016/j.lithos.2018.02.010

Ducea, M. N. (2011). Fingerprinting orogenic delamination. *geology* 39, 191–192. doi:10.1130/FOCUS022011.1

Feng, W. Y., and Zheng, J. H. (2021). Triassic magmatism and tectonic setting of the eastern Tianshan, NW China: Constraints from the Weiya intrusive complex. *lithos* 394, 106171–171. doi:10.1016/j.lithos.2021.106171

Gao, S., Rudnick, R. L., Yuan, H. L., Liu, X. M., Liu, Y. S., Xu, W. L., et al. (2004). Recycling lower continental crust in the North China craton. *Nature* 432, 892–897. doi:10.1038/nature03162

Gao, Z. W., Lü, C. L., Deng, M. g., Guan, S. J., and Yang, F. Q. (2021). Geochemical features and tectonic setting of the mesozoic intrusions in eastern tianshan. *Earth Sci.* 46, 2287–2298. doi:10.3799/dqkx.2020.212

Gillespie, J., Glorie, S., Xiao, W. J., Zhang, Z. Y., Collins, A. S., Evans, N., et al. (2017). Mesozoic reactivation of the beishan, southern central asian orogenic belt: Insights from low-temperature thermochronology. *Gondwana Res.* 43, 107–122. doi:10.1016/j.gr.2015.10.004

Griffin, W. L., Pearson, N. J., Belousova, E., Jackson, S. E., Achterbergh, E. V., O'Reilly, S. Y., et al. (2000). The Hf isotope composition of cratonic mantle: LAM-MC-ICPMS analysis of zircon megacrysts in kimberlites. *Geochim. Cosmochim. Acta* 64, 133–147. doi:10.1016/S0016-7037(99)00343-9

Griffin, W. L., Wang, X., Jackson, S. E., Pearson, N. J., O'Reilly, S. Y., Xu, X., et al. (2002). Zircon chemistry and magma mixing, SE China: *In-situ* analysis of Hf isotopes, tonglu and pingtan igneous complexes. *lithos* 61, 237–269. doi:10.1016/S0024-4937(02)00082-8

Guan, Q., Zhu, D. C., Zhao, Z. D., Dong, G. C., Zhang, L. L., Li, X. W., et al. (2012). Crustal thickening prior to 38Ma in southern Tibet: Evidence from lower crust-derived adakitic magmatism in the Gangdese Batholith. *Gondwana Res.* 21, 88–99. doi:10.1016/j.gr.2011.07.004

Han, C. M., Xiao, W. J., Zhao, G. C., Sun, M., Qu, W. J., and Du, A. D. (2014). Re-Os geochronology on molybdenites from the Donggebi Mo deposit in the eastern tianshan of the central asia orogenic belt and its geological significance. *Resour. Geol.* 64, 136–148. doi:10.1111/rge.12033

Han, Y. G., and Zhao, G. C. (2018). Final amalgamation of the tianshan and junggar orogenic collage in the southwestern central asian orogenic belt: Constraints on the closure of the Paleo-Asian ocean. *Earth Sci. Rev.* 186, 129–152. doi:10.1016/j.earscirev.2017.09.012

He, Z. Y., Klemd, R., Yan, L. L., Lu, T. Y., and Zhang, Z. M. (2018). Mesoproterozoic juvenile crust in microcontinents of the central asian orogenic belt: Evidence from oxygen and hafnium isotopes in zircon. *Sci. Rep.* 8, 5054. doi:10.1038/s41598-018-23393-4

Hou, K. J., Li, Y. H., Zou, T. R., Qu, X. M., Shi, Y. R., and Xie, G. Q. (2007). Laser ablation-MC-ICP-MS Technique for Hf isotope microanalysis of zircon and its geological applications. *Acta Geol. Sin.* 23, 2595–2604.

Hou, K. J., Tian, Y. R., and Li, Y. H. (2009). *In situ* U-Pb zircon dating using laser ablation-multi ion counting-ICP-MS. *Mineral. Deposits* 28, 481–492.

Hu, A. Q., Zhang, G. X., Zhang, Q. F., and Chen, Y. F. (1998). Constraints on the age of basement and crustal growth in Tianshan Orogen by Nd isotopic composition. *Sci. China (Series D)* 41, 648–657. doi:10.1007/BF02878748

Huang, X. L., Xu, Y. G., Lan, J. B., Yang, Q. J., and Luo, Z. Y. (2009). Neoproterozoic adakitic rocks from Mopanshan in the Western Yangtze Craton: Partial melts of a thickened lower crust. *lithos* 112, 367–381. doi:10.1016/j.lithos.2009.03.028

Huang, Z. Y., Long, X. P., Kroner, A., Yuan, C., Wang, Y. J., Chen, B., et al. (2015). Neoproterozoic granitic gneisses in the Chinese Central Tianshan Block: Implications for tectonic affinity and Precambrian crustal evolution. *Precambrian Res.* 269, 73–89. doi:10.1016/j.precamres.2015.08.005

Jahn, B. M., Wu, F. Y., and Chen, B. (2000). Granitoids of the central Asian orogenic belt and continental growth in the phanerozoic. *Earth Env. Sci. T. R. So.* 91, 181–193. doi:10.1017/S0263593300007367

Ju, Y. J., Zhang, X. L., Lai, S. C., and Qin, J. F. (2017). Permian-triassic highly-fractionated I-type granites from the southwestern qaidam basin (NW China): Implications for the evolution of the paleo-tethys in the eastern kunlun orogenic belt. *J. Earth Sci.* 28, 51–62. doi:10.1007/s12583-017-0745-5

Le Bas, M. J., Le Maitre, R. W., Streckeisen, A., and Zanettin, B. (1986). A chemical classification of volcanic rocks based on the total alkali-silica diagram. *J. Petrology* 27, 745–750. doi:10.1093/petrology/27.3.745

Lei, R. X., Brzozowski, M. J., Feng, Y. G., Zhang, K., Muhtar, M., Luo, X. L., et al. (2021). Triassic crust-mantle interaction in the Eastern Tianshan, southern Altaids: Insights from microgranular enclaves and their host Tianhu granitoids. *lithos* 402, 105879. doi:10.1016/j.lithos.2020.105879

Lei, R. X., Wu, C. Z., Gu, L. X., Zhang, Z. Z., Chi, G. X., and Jiang, Y. H. (2011). Zircon U–Pb chronology and Hf isotope of the Xingxingxia granodiorite from the Central Tianshan zone (NW China): Implications for the tectonic evolution of the southern Altaids. *Gondwana Res.* 20, 582–593. doi:10.1016/j.gr.2011.02.010

Lei, R. X., Wu, C. Z., Zhang, Z. Z., and Gu, L. X. (2013). Geochronology, geochemistry and tectonic significances of the Yamansubei pluton in eastern Tianshan, Northwest China. *Acta Petrol. Sin.* 29, 2653–2664.

Li, D. F., Zhang, L., Chen, H. Y., Hollings, P., Cao, M. J., Fang, J., et al. (2016). Geochronology and geochemistry of the high Mg dioritic dikes in Eastern Tianshan, NW China: Geochemical features, petrogenesis and tectonic implications. *J. Asian Earth Sci.* 115, 442–454. doi:10.1016/j.jseaes.2015.10.018

Li, N., Yang, F. Q., Zhang, Z. X., and Yang, C. D. (2019). Geochemistry and chronology of the biotite granite in the Xiaobaishitou W-(Mo) deposit, eastern Tianshan, China: Petrogenesis and tectonic implications. *Ore Geol. Rev.* 107, 999–1019. doi:10.1016/j.oregeorev.2019.03.027

Li, S., Wang, T., Wilde, S. A., and Tong, Y. (2013). Evolution, source and tectonic significance of Early Mesozoic granitoid magmatism in the Central Asian Orogenic Belt (central segment). *Earth Sci. Rev.* 126, 206–234. doi:10.1016/j.earscirev.2013.06.001

Li, S., Wang, T., Wilde, S. A., Tong, Y., Hong, D. W., and Guo, Q. Q. (2012). Geochronology, petrogenesis and tectonic implications of Triassic granitoids from Beishan, NW China. *lithos* 134-135, 123–145. doi:10.1016/j.lithos.2011.12.005

Liao, X. D., Sun, S., Chi, H. Z., Jia, D. Y., Nan, Z. Y., and Zhou, W. N. (2019). The late permian highly fractionated I-type granites from sishijia pluton in southestern inner Mongolia, north China: A post-collisional magmatism record and its implication for the closure of Paleo-Asian ocean. *lithos* 328-329, 262–275. doi:10.1016/j.lithos.2019.01.027

Liu, S. Y., Wang, R., Jeon, H., Hou, Z. Q., Xue, Q. W., Zhou, L. M., et al. (2020). Indosinian magmatism and rare metal mineralization in East Tianshan orogenic belt: An example study of Jingerquan Li-Be-Nb-Ta pegmatite deposit. *Ore Geol. Rev.* 116, 103265. doi:10.1016/j.oregeorev.2019.103265

Liu, Y. S., Gao, S., Hu, Z. C., Gao, C. G., Zong, K. Q., and Wang, D. B. (2010). Continental and oceanic crust recycling-induced melt-peridotite interactions in the trans-north China orogen: U-Pb dating, Hf isotopes and trace elements in zircons from mantle xenoliths. *J. Petrology* 51, 537–571. doi:10.1093/PETROLOGY/EGP082

Long, X. P., Wilde, S. A., Wang, Q., Yuan, C., Wang, X. C., Li, J., et al. (2015). Partial melting of thickened continental crust in central Tibet: Evidence from geochemistry and geochronology of Eocene adakitic rhyolites in the northern Qiangtang Terrane. *Earth Planet. Sci. Lett.* 414, 30–44. doi:10.1016/j.epsl.2015.01.007

Long, X. P., Wu, B., Sun, M., Yuan, C., Xiao, W. J., and Zuo, R. (2020). Geochronology and geochemistry of late carboniferous dykes in the aqishan-yamansu belt, eastern tianshan: Evidence for a post-collisional slab breakoff. *Geosci. Front.* 11, 347–362. doi:10.1016/j.gsf.2019.06.003

Ludwig, K. R. (2003). User's manual for isoplot/ex version 3: A geochronological toolkit for microsoft excel. *Spec. Publ.* 4, 1–70.

Luo, B. J., Zhang, H. F., and Lü, X. B. (2012). U-Pb zircon dating, geochemical and Sr-Nd-Hf isotopic compositions of early indosinian intrusive rocks in west qinling, central China: Petrogenesis and tectonic implications. *Contrib. Mineral. Pet.* 164, 551–569. doi:10.1007/s00410-012-0748-2

Maniar, P. D., and Piccoli, P. M. (1989). Tectonic discrimination of granitoids. *Geol. Soc. Am. Bull.* 101, 635–643. doi:10.1130/0016-7606(1989)1012.3.CO;2

Ma, X. X., Shu, L. S., Meert, J. G., and Li, J. Y. (2014). The paleozoic evolution of central tianshan: Geochemical and geochronological evidence. *Gondwana Res.* 25, 797–819. doi:10.1016/j.gr.2013.05.015

Mao, L. J., He, Z. Y., Zhang, Z. M., Klemd, R., Xiang, H., Tian, Z. L., et al. (2015). Origin and geodynamic significance of the early mesozoic Weiya LP and HT granulites from the Chinese eastern tianshan. *lithos* 239, 142–156. doi:10.1016/j.lithos.2015.10.016

Mao, Q. G., Ao, S. J., Windley, B. F., Wang, J. B., Li, Y. C., and Xiao, W. J. (2021). Middle Triassic lower crust-derived adakitic magmatism: Thickening of the Dananhu intra-oceanic arc and its implications for arc-arc amalgamation in the Eastern Tianshan (NW China). *Geol. J.* 56, 3137–3154. doi:10.1002/gj.4095

Mao, Q. G., Ao, S. J., Windley, B. F., Zhang, Z. Y., Sang, M., Tan, Z., et al. (2022). Middle-late triassic southward-younging granitoids: Tectonic transition from subduction to collision in the eastern tianshan-beishan orogen, NW China. *Geol. Soc. Am. Bull.* 134, 2206–2224. doi:10.1130/B36172.1

Martin, H. (1999). Adakitic magmas: Modern analogues of archaean granitoids. *lithos* 46, 411–429. doi:10.1016/S0024-4937(98)00076-0

Muhtar, M. N., Wu, C. Z., Santosh, M., Lei, R. X., Feng, Y. G., Yang, T., et al. (2020). Peraluminous granitoid magmatism from isotopically depleted sources: The case of Jing'erquanbei pluton in Eastern Tianshan, Northwest China. *Geol. J.* 55, 117–132. doi:10.1002/gj.3392

Pearce, J. A., Harris, N. B. W., and Tindle, A. G. (1984). Trace element discrimination diagrams for the tectonic interpretation of granitic rocks. *J. Petrology* 25, 956–983. doi:10.1093/petrology/25.4.956

Peccerillo, A., and Taylor, S. R. (1976). Geochemistry of Eocene calc-alkaline volcanic rocks from the Kastamonu area, Northern Turkey. *Contrib. Mineral. Pet.* 58, 63–81. doi:10.1007/BF00384745

Rapp, R. P., Shimizu, N., Norman, M. D., and Applegate, G. S. (1999). Reaction between slab-derived melts and peridotite in the mantle wedge: Experimental constraints at 3.8 GPa. *Chem. Geol.* 160, 335–356. doi:10.1016/S0009-2541(99)00106-0

Roberts, M. P., and Clemens, J. D. (1993). Origin of high-potassium, calc-alkaline, I-type granitoids. *geology* 21, 825–828. doi:10.1130/0091-7613(1993)021<0825:OOHPTA>2.3.CO;2

Rudnick, R. L., and Fountain, D. M. (1995). Nature and composition of the continental crust: A lower crustal perspective. *Rev. Geophy.* 33, 267–309. doi:10.1029/95RG01302

Scherer, E., Münker, C., and Mezger, K. (2001). Calibration of the lutetium-hafnium clock. *Science* 293, 683–687. doi:10.1126/science.1061372

Sisson, T., Ratajeski, K., Hankins, W., and Glazner, A. (2005). Voluminous granitic magmas from common basaltic sources. *Contrib. Mineral. Pet.* 148, 635–661. doi:10.1007/s00410-004-0632-9

Song, S. G., Wang, M. J., Wang, C., and Niu, Y. L. (2015). Magmatism during continental collision, subduction, exhumation and mountain collapse in collisional orogenic belts and continental net growth: A perspective. *Sci. China Earth Sci.* 58, 1284–1304. doi:10.1007/s11430-015-5102-x

Su, B. X., Sakyi, P. A., Malaviarachchi, S., Li, X. H., Yang, Y. H., Sun, H., et al. (2011). U-Pb ages and Hf-O isotopes of zircons from Late Paleozoic mafic–ultramafic units in the southern Central Asian Orogenic Belt: Tectonic implications and evidence for an Early-Permian mantle plume. *Gondwana Res.* 20, 516–531. doi:10.1016/j.gr.2010.11.015

Sun, H. S., Li, H., Danišík, M., Xia, Q. L., Jiang, C. L., Wu, P., et al. (2017). U-Pb and Re-Os geochronology and geochemistry of the Donggebi Mo deposit, Eastern Tianshan, NW China: Insights into mineralization and tectonic setting. *Ore Geol. Rev.* 86, 584–599. doi:10.1016/j.oregeorev.2017.03.020

Sun, S. S., and McDonough, W. F. (1989). Chemical and isotopic systematics of oceanic basalts: Implications for mantle composition and processes. *Geol. Soc. Lond. Spec. Publ.* 42, 313–345. doi:10.1144/GSL.SP.1989.042.01.19

Wang, B., Chen, Y., Zhan, S., Shu, L. s., Faure, M., Cluzel, D., et al. (2007). Primary carboniferous and permian paleomagnetic results from the yili block (NW China) and their implications on the geodynamic evolution of Chinese tianshan belt. *Earth Planet. Sci. Lett.* 263, 288–308. doi:10.1016/j.epsl.2007.08.037

Wang, B., Cluzel, D., Jahn, B. M., Shu, L. S., Chen, Y., Zhai, Y. Z., et al. (2014). Late Paleozoic pre- and syn-kinematic plutons of the Kangguer-Huangshan Shear zone: Inference on the tectonic evolution of the eastern Chinese north Tianshan. *Am. J. Sci.* 314, 43–79. doi:10.2475/01.2014.02

Wang, Q., Hawkesworth, C. J., Wyman, D., Chung, S. L., Wu, F. Y., Li, X. H., et al. (2016a). Pliocene-Quaternary crustal melting in central and northern Tibet and insights into crustal flow. *Nat. Commun.* 7, 11888–11911. doi:10.1038/ncomms11888

Wang, T., Li, W. P., Li, J. B., Hong, D. W., Tong, Y., and Shan, L. (2008). Increase of juvenal mantle-derived composition from syn-orogenic to post-orogenic granites of the east part of the eastern tianshan (China) and implications for continental vertical growth: Sr and Nd isotopic evidence. *Acta Petrol. Sin.* 24, 762–772.

Wang, Y. H., Xue, C. J., Liu, J. J., and Zhang, F. F. (2016b). Geological, geochronological, geochemical, and Sr-Nd-O-Hf isotopic constraints on origins of intrusions associated with the Baishan porphyry Mo deposit in eastern Tianshan, NW China. *Miner. Deposita* 51, 953–969. doi:10.1007/s00126-016-0646-z

Wang, Y. H., Xue, C. J., Wang, J. P., Peng, R. M., Yang, J. T., Zhang, F. F., et al. (2015a). Petrogenesis of magmatism in the yandong region of eastern tianshan, Xinjiang: Geochemical, geochronological, and Hf isotope constraints. *Int. Geol. Rev.* 57, 1130–1151. doi:10.1080/00206814.2014.900653

Wang, Y. H., Zhang, F. F., Liu, J. J., Xue, C. J., Wang, J. P., Liu, B., et al. (2015b). Petrogenesis of granites in Baishan molybdenum deposit, eastern Tianshan, Xinjiang: Zircon U-Pb geochronology, geochemistry, and Hf isotope constraints. *Acta Petrol. Sin.* 31, 1962–1976.

Wang, Y., Sun, G., and Li, J. (2010). U-Pb (shrimp) and $^{40}Ar/^{39}Ar$ geochronological constraints on the evolution of the Xingxingxia shear zone, NW China: A triassic segment of the altyn tagh fault system. *Geol. Soc. Am. Bull.* 122, 487–505. doi:10.1130/B26347.1

Whalen, J. B., Currie, K. L., and Chappell, B. W. (1987). A-type granites: Geochemical characteristics, discrimination and petrogenesis. *Contrib. Mineral. Pet.* 95, 407–419. doi:10.1007/bf00402202

Wu, C. Z., Zhang, Z. Z., Gu, L. X., Tang, J. H., and Lei, R. X. (2010). Sr, Nd and O isotopic characters of quartz syenite in the Weiya magmatic complex from eastern Tianshan in NW China: Melting of the thickened juvenile lower crust. *Geochem. J.* 44, 285–298. doi:10.2343/geochemj.1.0072

Wu, F. Y., Liu, Z. C., Liu, X. C., and Ji, W. Q. (2015). Himalayan leucogranite: Petrogenesis and implications to orogenesis and plateau uplift. *Acta Petrol. Sin.* 31, 1–36.

Wu, Y. S., Xiang, N., Tang, H. S., Zhou, K. F., and Yang, Y. F. (2013). Molybdenite Re-Os isotope age of the Donggebi Mo deposit and the Indosinian metallogenic event in eastern Tianshan. *Acta Geol. Sin.* 29, 121–130.

Wu, Y. S., Zhou, K. F., Li, N., and Chen, Y. J. (2017). Zircon U-Pb dating and Sr-Nd-Pb-Hf isotopes of the ore-associated porphyry at the giant Donggebi Mo deposit, Eastern Tianshan, NW China. *Ore Geol. Rev.* 2, 794–807. doi:10.1016/j.oregeorev.2016.02.007

Wyborn, D., Chappell, B. W., and James, M. (2001). Examples of convective fractionation in high-temperature granites from the Lachlan Fold Belt. *Aust. J. Earth Sci.* 48, 531–541. doi:10.1046/j.1440-0952.2001.00877.x

Xiao, W. J., Han, C. M., Yuan, C., Sun, M., Lin, S., Chen, H., et al. (2008). Middle cambrian to permian subduction-related accretionary orogenesis of northern Xinjiang, NW China: Implications for the tectonic evolution of central asia. *J. Asian Earth Sci.* 32, 102–117. doi:10.1016/j.jseaes.2007.10.008

Xiao, W. J., Windley, B. F., Allen, M. B., and Han, C. M. (2013). Paleozoic multiple accretionary and collisional tectonics of the Chinese Tianshan orogenic collage. *Gondwana Res.* 23, 1316–1341. doi:10.1016/j.gr.2012.01.012

Xiao, W. J., Zhang, L. C., Qin, K. Z., Sun, S., and Li, J. L. (2004). Paleozoic accretionary and collisional tectonics of the Eastern Tianshan (China): Implications for the continental growth of central Asia. *Am. J. Sci.* 304, 370–395. doi:10.2475/ajs.304.4.370

Yuan, C., Zhou, M. F., Sun, M., Zhao, Y. J., Wilde, S., Long, X. P., et al. (2010). Triassic granitoids in the eastern Songpan Ganzi Fold Belt, SW China: Magmatic response to geodynamics of the deep lithosphere. *Earth Planet. Sci. Lett.* 290, 481–492. doi:10.1016/j.epsl.2010.01.005

Zhang, D. Y., Zhou, T. F., Yuan, F., Xiao, W. J., White, N. C., Deng, Y. F., et al. (2015a). Petrogenesis and mineralization potential of a granite porphyry intrusion beneath the Baishan Mo deposit, Eastern Tianshan, NW China. *J. Asian Earth Sci.* 113, 254–265. doi:10.1016/j.jseaes.2015.05.002

Zhang, L. C., Qin, K. Z., and Xiao, W. J. (2008). Multiple mineralization events in the eastern Tianshan district, NW China: Isotopic geochronology and geological significance. *J. Asian Earth Sci.* 32, 236–246. doi:10.1016/j.jseaes.2007.10.011

Zhang, X. R., Zhao, G. C., Eizenhöfer, P. R., Sun, M., Han, Y. G., Hou, W. Z., et al. (2016a). Late Ordovician adakitic rocks in the Central Tianshan block, NW China: Partial melting of lower continental arc crust during back-arc basin opening. *Geol. Soc. Am. Bull.* 128, 1367–1382. doi:10.1130/B31452.1

Zhang, X. R., Zhao, G. C., Eizenhöfer, P. R., Sun, M., Han, Y. G., Hou, W. Z., et al. (2015b). Latest Carboniferous closure of the Junggar Ocean constrained by geochemical and zircon U-Pb-Hf isotopic data of granitic gneisses from the Central Tianshan block, NW China. *lithos* 238, 26–36. doi:10.1016/j.lithos.2015.09.012

Zhang, X. R., Zhao, G. C., Eizenhöfer, P. R., Sun, M., Han, Y. G., Hou, W. Z., et al. (2016b). Tectonic transition from Late Carboniferous subduction to Early Permian post-collisional extension in the Eastern Tianshan, NW China: Insights from geochronology and geochemistry of mafic-intermediate intrusions. *lithos* 256-257, 269–281. doi:10.1016/j.lithos.2016.04.006

Zhang, X. R., Zhao, G. C., Sun, M., Eizenhöfer, P. R., Han, Y. G., Hou, W. Z., et al. (2016c). Tectonic evolution from subduction to arc-continent collision of the Junggar ocean: Constraints from U-Pb dating and Hf isotopes of detrital zircons from the North Tianshan belt, NW China. *Geol. Soc. Am. Bull.* 128, 644–660. doi:10.1130/B31230.1

Zhang, X. R., Zhao, G. C., Sun, M., Han, Y. G., and Liu, Q. (2017). Triassic magmatic reactivation in Eastern Tianshan, NW China: Evidence from geochemistry and zircon U-Pb-Hf isotopes of granites. *J. Asian Earth Sci.* 145, 446–459. doi:10.1016/j.jseaes.2017.06.022

Zhang, Z. Z., Gu, L. X., Wu, C. Z., Li, W. Q., Xi, A. H., and Wang, S. (2005). Zircon SHRIMP dating for the Weiya pluton, Eastern Tianshan: Its geological implications. *Acta Geol. Sin.* 79, 481–490. doi:10.1111/j.1755-6724.2005.tb00914.x

Zhang, Z. Z., Gu, L. X., Wu, C. Z., Zhai, J. P., Li, W. Q., and Tang, J. H. (2007). Early indosinian Weiya gabbro in eastern tianshan, China: Elemental and Sr-Nd-O isotopic geochemistry, and its tectonic implications. *Acta Geol. Sin. Engl. Ed.* 81, 424–432. doi:10.1111/j.1755-6724.2007.tb00965.x

Zhao, H. G., Rui, S. U., Liang, J. W., Wang, J., Jin, Y. X., Ou, G. X., et al. (2017). Petrology, geochemical characteristics and Genesis of the Tianhu pluton in the east section of the middle Tianshan Mountains. *Acta Geol. Sin.* 91, 1028–1226.

Zhao, H. G., Su, R., Liang, J. W., Jin, Y. X., Ou, G. X., and Jiang, X. H. (2018). Petrological and geochemical characteristics of the Yamansu pluton in the qoltag area, east tianshan mountaints and their intra-continental tectonic significance. *Acta Geol. Sin.* 92, 1780–1802.

Zhao, L. D., Chen, H. Y., Hollings, P., and Han, J. S. (2019). Tectonic transition in the aqishan-yamansu belt, eastern tianshan: Constraints from the geochronology and geochemistry of carboniferous and triassic igneous rocks. *lithos* 344-345, 247–264. doi:10.1016/j.lithos.2019.06.023

Zhi, J., Lei, R., Chen, B., Muhtar, M. N., Feng, Z., Zhang, K., et al. (2021). Zircon genesis and geochronology for the zhangbaoshan super-large rubidium deposit in the eastern tianshan, NW China: Implication to magmatic-hydrothermal evolution and mineralization processes. *Front. Earth Sci.* 9, 682720. doi:10.3389/feart.2021.682720

Zhou, T. F., Feng, Y., Zhang, D. Y., Yu, F., Liu, S., Peng, M. X., et al. (2010). Geochronology, tectonic setting and mineralization of granitoids in Jueluotage area, eastern Tianshan, Xinjiang. *Acta Petrol. Sin.* 26, 478–502.

Zhu, D. C., Mo, X. X., Wang, L. Q., Zhao, Z. D., Niu, Y. L., Zhou, C. Y., et al. (2009). Petrogenesis of highly fractionated I-type granites in the Zayu area of eastern Gangdese, Tibet: Constraints from zircon U-Pb geochronology, geochemistry and Sr-Nd-Hf isotopes. *Sci. China Ser. D Earth Sci.* 52, 1223–1239. doi:10.1007/s11430-009-0132-x